

Precise Estimates of Ocean Surface Parameters from the CryoSat-2 Synthetic Aperture, Interferometric Altimeter.

Katharine A. Giles, Duncan J. Wingham, Natalia Galin, Member IEEE, Robert Cullen and Walter H. F. Smith.

Abstract—This paper examines the performance of measurements of ocean surface height, surface roughness, and across-track surface slope of the CryoSat-2 ‘SIRAL’ altimeter in ‘SARIN’ and ‘SAR’ operational modes. Through interrupting SAR mode processing upstream of synthetic aperture formation, a comparison is made with the performance of SIRAL in a conventional, pulse-limited configuration. Description of the model of SARIN mode interferometric echo cross-product, and SARIN mode, SAR mode and pulse-limited powers is given. These models use the smallness of the pitch and roll of the satellite, and limited range of satellite altitude to provide a semi-analytic echo model, whose numerical dimensions limited to two, or in the case of SARIN mode at large roll angles, three dimensions, make practical their application to extensive data. A theoretical description of the fluctuations in the multi-looked, SARIN cross-product, and SARIN, SAR and pulse-limited powers is given, by extending the models to describe correlations between individual looks in the SARIN, SAR and pulse-limited cases. The theoretical predictions are compared to fluctuations observed in practice. Measurements of ocean surface parameters obtained from CryoSat-2 observations over the Pacific and Atlantic oceans are reported. We show that unbiased estimates of the across-track slope can be obtained; and that there are no observable biases between SAR mode and pulse-limited measurements observed at the same location and time. The precision of the SAR mode and pulse-limited measurements are compared, and demonstrate that a future SAR altimeter designed to optimize the number of looks offers superior performance to pulse-limited satellite altimetry.

Index Terms—radar altimetry, spaceborne radar, synthetic aperture radar, radar remote sensing, ocean surface, geophysical sea measurements.

Manuscript received October 11th, 2013; revised Month XX, YYYY; accepted Month XX, YYYY. Date of publication Month XX, YYYY; date of current version August XX, 2013.

D.J. Wingham is, and K.A. Giles was (prior to her death on April 10, 2013) at the Centre for Polar Observation and Modelling (CPOM), Department of Earth Sciences, University College London, London WC1E 6BT (email: djw@cpom.ucl.ac.uk)

N. Galin and W.H.F. Smith are with the Laboratory for Satellite Altimetry, at the National Oceanic and Atmospheric Administration, College Park, MD 20740, United States (e-mails: natalia.galin@noaa.gov and walter.hf.smith@noaa.gov)

Robert Cullen is with ESA/ESTEC, 1 Keplerlaan, Noordwijk, Netherlands (email: Robert.Cullen@esa.int)

I. INTRODUCTION

FOR MORE than three decades, satellite altimetry has provided a wealth of information concerning the marine gravity field (e.g. [1] [2]), the ocean dynamic topography (e.g., [3]) and its variability (e.g., [4] [5]) ocean tides (e.g. [6]), the height of the ocean swell waves [7], and the ocean surface wind speed [8]. Successive satellites, from Seasat (1978) onwards, have had radar altimeters among their payload, and the use of radar altimeter observations in operational forecasting of ocean dynamics, waves and winds is now familiar and well established [9], [10], [11].

While the intervening period has seen a continued improvement in the accuracy and precision of satellite altimeter measurements, arising variously from the improvement in gravity modeling and microwave tracking systems ([12], [13]) increases in the pulse repetition frequency [14], the introduction of dual frequency measurements (e.g., [14], [15]), and of solid state power amplification [16] the design of radar altimeters has not altered greatly from that of Seasat [17], [18]: a normal incidence, full-deramp 13.6 GHz radar with a circular antenna of around 1 m diameter using a 320 MHz bandwidth chirp. Similarly, the ocean surface parameters derived from these measurements use, essentially, the model of the normal incidence scattering of the sea surface developed at the time and expressed in a closed form by [19].

Despite a design aimed at measuring the properties of the ocean surface, pulse-limited altimeters have also provided new insights into the behavior of the large ice sheets of Antarctica (e.g. [20]) and Greenland [21], and, more recently, Arctic sea ice at the synoptic scale [22]. Nonetheless, the more variable topography of ice sheets, and the scattering inhomogeneity of sea ice interspersed with leads, has limited their performance and (along with the choice of orbit inclination) their coverage. For these reasons, the CryoSat-2 satellite [23], whose primary mission goal is to observe fluctuations in Earth’s marine and continental ice fields, has its main payload, the ‘SIRAL’ altimeter, which differs in design from earlier, pulse-limited altimeters. It exploits a design used first in planetary satellite missions [24], that, through improving the spatial resolution with along-track aperture synthesis, better distinguishes sea ice floes from the intervening leads; and, as proposed by [25], adds a second altimeter in the across-track direction, with

which the slopes of the marginal regions of the continental ice sheets can be determined.

However, it has been argued for some time [26], [27], that a synthetic aperture altimeter might also offer a greater measurement precision over the open ocean than does the pulse-limited design. In addition, the calibration of the CryoSat-2 interferometer has demonstrated sufficient accuracy to measure the across-track slope of the ocean surface [28]. For these reasons, limited acquisitions of so-called ‘SARIN mode’ data, for which phase coherent transmissions at a sufficient pulse-repetition interval makes synthetic aperture synthesis possible, and ‘SARIN mode’ data, for which in addition measurements with the second antenna are made, have been obtained over the world’s oceans, in order that the potential merits of synthetic aperture altimetry of the ocean can be assessed. In addition, in SARIN and SAR modes, the synthetic aperture process is performed on ground, and by interrupting this process prior to aperture formation, pulse-limited observations can be obtained of the same ocean, at the same time, as those obtained from the aperture-synthesised, SARIN or SAR-mode echoes. This is used, in this paper, to make a direct comparison of the performance of SAR mode and pulse-limited measurements.

In this paper, the performance of the CryoSat-2 range, wave-height and across-track slope measurements is assessed over the open ocean, in so far as it depends on the echo shapes (we do not consider variations due to uncertain altitude and the speed of light through the atmosphere). There are two aspects of importance in this connection. The first of these is accuracy, by which we mean the degree to which the measurements are biased. Unbiased estimates require a detailed model of the echo power, or, in the case of the interferometer, the echo cross-product, and its dependence on the surface parameters. We take as a suitably accurate model of the SARIN echo cross-product, and SARIN and SAR mode echo powers, the description of [29], together with the modifications particular to CryoSat-2, such as the ellipticity of its antennas, given by [28]. As described there, however, that model would require numerical look-up tables of considerable size and dimensionality to apply in practice, and in section II, the smallness of the satellite pitch and roll, and the limited range of satellite altitude is exploited to reduce the size of the look up tables that are required in practice to two, or in the SARIN case, three) dimensions. By simple modifications, the pulse-limited model is obtained as a special case of the SAR mode echo model.

The second aspect is that of precision, by which we mean the random fluctuation in the measurements arising from the presence of radar speckle. As with pulse-limited altimetry, this depends to the extent to which individual echoes that are gathered prior to multi-looking are correlated. However, in addition, SAR (and SARIN) altimetry is distinct from pulse limited altimetry in that the multi-looking is also performed from individual echoes drawn from different statistical populations. In section III, these aspects are examined through determining the effective number of looks – a measure of the effectiveness of the multi-looking in suppressing speckle

fluctuations – in the SARIN and SAR modes, and compare these with that provided by pulse-limited operation. For this purpose the models of section II are extended to include the correlation properties of the echoes in addition to their means. This section is concluded with a comparison of the modeled effective number of looks with that observed in practice.

In section IV, the results of these sections are applied to examine the measurements of ocean surface height, across-track slope and significant wave height. It is demonstrated in particular how the model of the SARIN cross-product developed in section II results in bias free estimates of the ocean across-track surface slope, and the precision of the across track surface slope measurement is determined. We then turn to the SAR mode measurements, and in particular demonstrate that, with the use of the models in section II, the measurements obtained in SAR mode and pulse-limited operation have no distinguishable relative bias, so that, measurements made by a future SAR mode mission would be completely compatible with those of past, pulse-limited missions. Finally, the relative precision of the SAR mode and pulse-limited measurements is examined. It is shown that while the precision of the SAR measurement is superior, this is a simply a contingent consequence of the correlation behavior of the pulse-limited echoes when the instrument is operated in pulse-limited modes. On the other hand, the results support the contention that were an altimeter to be designed so as to optimize the number of looks, as suggested by [30], an improvement can be expected in precision over that obtained historically with 13.6 GHz pulse-limited radar altimeters.

Finally, three appendices to the paper provide (appendix A) a detailed description of the data that was used in this study; the details (appendix B) of the data processing we applied to obtain the results provided in the main text; and (appendix C) details of the effect of the attitude rate on the echo shape.

II. MODELS OF THE MEAN ECHO CROSS-PRODUCT AND ECHO POWER.

In general, the aim of the CryoSat-2 altimeter measurement over the ocean is to determine the values of the ocean surface height, parameterized by a delay time τ_0 in the echo, the across-track gradient, parameterized by an ‘interferometer angle’ θ in the interferometer echo cross-product (described more fully below) the ocean backscattering coefficient σ^0 (from which wind-speed is estimated) that depends on the received echo power, and the standard deviation σ_s of the surface height distribution (from which the wave height is estimated), obtained from the slope on the echo leading edge. To do so, samples of the echo power are fit to a model $p_r(\sigma^0, \sigma_s; \tau - \tau_0)$ of the variation of echo power, or of the echo cross-product to a model $\Psi_r(\sigma^0, \sigma_s, \theta; \tau - \tau_0)$ of the echo cross-product, by finding the values $\tilde{\tau}_0, \tilde{\sigma}^0, \tilde{\sigma}_s$ and $\tilde{\theta}$ of the parameters that minimize the weighted, least-squares difference between the samples and the model.

In addition to the ocean parameters, the echo power is also sensitive to parameters that characterize the measurement

system (detailed in [28]) and which vary from echo to echo: the measurement altitude, the antenna pointing, generally in the case of CryoSat-2 requiring two angles to specify it, and, in the case of ‘SAR’ and ‘SARIN’ mode echoes, the velocity of the satellite. Thus, generally, the echo power is a seven- or a nine-dimensional function.

Were the models analytic, this presents no particular difficulty, but when, as is the case here, the model can only be ‘exactly’ determined numerically, the high dimensionality presents a challenge in its computation if not its application. Thus, it is helpful if, to the greatest extent possible, the smallness of the variations in some parameters can be exploited to reduce the dimensionality of the functions that need numerical calculation. This is the aim of this section, in which we reduce the numerical dimensionality of the functions used in the ‘SAR’ and pulse-limited echo models to two dimensions, and that for the ‘SARIN’ echo or cross-product to three. We work by discussing first the SARIN echo cross-product model, and then, by successive simplifications, the SAR and finally pulse-limited models.

A. The cross-product impulse response.

In general, the mean echo cross-product Ψ at near normal incidence from a rough surface is described by the triple convolution

$$\Psi_r(\tau) = p_t(\tau) * p_z(\tau) * X(\tau, B) , \quad (1)$$

where p_t is the compressed pulse shape (also known as the ‘single point-target response’) p_z is the surface elevation probability density function, and X is the cross-product ‘impulse response’ of the surface. X is a function of delay and interferometer baseline B . If (1) is evaluated for zero baseline, the result is the echo power:

$$p_r(\tau) = p_t(\tau) * p_z(\tau) * X(\tau, 0) . \quad (2)$$

The decomposition (2) is due to [19] who introduced the impulse response to describe the echo power; the extension of (1) to the echo cross-product involves no new assumptions.

The theoretical description of the interferometer echo cross-product we use is that of [29], in the form tailored to the parameters of the SIRAL altimeter given in [28]. Fig. 1 shows the along and across-track geometry of the radar imaging.

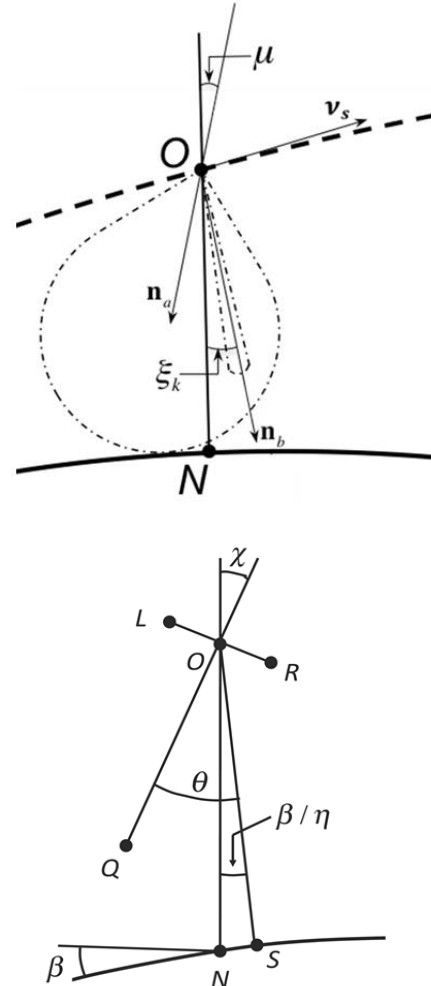


Fig. 1. The (upper panel) along-track, and (lower panel) across-track geometry of the radar imaging. The satellite proceeds along its orbit (dashed line in (a)). At any point on the orbit O , the satellite lies normally above the ellipsoidal nadir point N . The velocity vector \mathbf{v}_s lies tangential to the orbit at O . The antennas’ bore-sight direction \mathbf{n}_a is generally pitched at an angle μ to the nadir direction. (When the satellite is pitched and rolled, as shown in the lower panel \mathbf{n}_a has a component in the across-track direction.) Synthetic beams (only one is shown for clarity) are formed at a sequence of look angles ξ_k that describe the angle between the synthetic beam bore-sight direction \mathbf{n}_b and the nadir direction. In the across-track direction, the transmitting antenna (L for the SIRAL ‘A’ chain used in this paper) falls on the left when viewed in the direction of flight. In SAR mode, the left antenna is used for reception; in SARIN mode the left and right (R) antennas are used for reception. The antennas’ baseline normal direction (OQ) is generally rolled by an angle χ with respect to the nadir direction. The ‘interferometer’ angle θ can be interpreted geometrically as the angle of the first arrival, measured from the baseline normal, at the satellite of an echo from a surface with an across-track slope β relative to the ellipsoid. Due to the Earth’s curvature, the surface angle perceived by the interferometer is smaller than β by the factor η .

The multi-looked cross-product impulse-response from a surface slightly inclined to a sphere when using a mispointed, elliptical antenna is

$$X(\tau, B) \sim \sum_{k=-\frac{(N-1)}{2}}^{\frac{(N-1)}{2}} X_k(\tau, B) \quad (3)$$

where

$$X_k(\tau, B) \sim \frac{\lambda^2 G_0^2 D_0 c \sigma^0}{32\pi^2 h^3 \eta} H\left(\tau + \frac{\eta h \xi_k^2}{c}\right) e^{-ik_0 B (\chi + \beta/\eta)} \int_0^{2\pi} d\vartheta d(\rho_k \cos\vartheta - \xi_k) e^{ik_0 B \rho_k \sin\vartheta} \cdot \exp\left[-2\left(\frac{(\rho_k \cos\vartheta - \mu - \varsigma/\eta)^2}{\gamma_1^2} + \frac{(\rho_k \sin\vartheta - \chi - \beta/\eta)^2}{\gamma_2^2}\right)\right]. \quad (4)$$

X_k are the cross-product impulse responses of individual beams.

In (4), λ is the carrier wavelength and k_0 its wavenumber, c is the speed of light, and h is the satellite altitude. H is the Heaviside step-function. The parameter $\eta = 1 + h/R$, where R is the Earth radius, is a geometric factor that arises because the surface is spherical rather than plane.

Eqn. (4) employs the description

$$G_0 \exp\left[-\psi^2\left(\frac{\cos^2\omega}{\gamma_1^2} + \frac{\sin^2\omega}{\gamma_2^2}\right)\right] \quad (5)$$

for the antennas' gain pattern, in which ψ is the polar angle measured from the antennas' boresight, and ω is the azimuthal angle, measured from the along-track direction. γ_1 and γ_2 determine the along- and across-track width of the illumination. μ and χ are the pitch and roll angles respectively of the antennas, and ς and β are the along- and across-track components of the surface vector gradient.

D_0 is the one-way gain of a synthetic beam, and $d(\xi)$ is its pattern at an angle ξ from its boresight in the along-track direction. ξ_k is the along-track direction of the boresight of the k^{th} synthetic beam measured from the nadir direction. (See fig. 1). We term ξ_k the 'look angle' of the beam. Its value is

$$\xi_k = k\pi/(N_a k_0 v_s \Delta_t) \quad (6)$$

where N_a is the number of samples in the synthetic aperture, k_0 is the carrier wavenumber v_s is the magnitude of the satellite velocity in an Earth-fixed frame, and Δ_t is the pulse-repetition interval of the synthetic aperture. (Appendix A describes the transmission sequence in more detail.)

In general, we denote the number of looks that form a multi-looked echo by N . (To distinguish it later from a second measure, we will sometimes also describe N as the 'actual' number of looks.) In the SAR and SARIN modes, this is equal to the number of look angles, and in these cases N is given by

$$N = \pi h \eta / (k_0 v_s^2 \Delta_t \Delta_b) \quad (7)$$

Here, Δ_b is the 'burst' repetition interval, that is, the interval between successive synthetic apertures.

Δ_b takes different values in the SARIN and SAR modes so that the number of looks is not equal in the two modes, and we will distinguish these by N_S and N_{SI} where necessary. In the pulse-limited case, the corresponding number of looks is $N_P = 4N_a$.

The parameter ρ_k in (4) is given by

$$\rho_k = \sqrt{\frac{c\tau}{\eta h} + \xi_k^2} \quad (8)$$

(8) accounts for the 'slant range correction' given by eqn. 27 of [29].

The dependence of the impulse response on the spacecraft attitude is of the form $X(\mu + \varsigma/\eta, \chi + \beta/\eta)$. This is a consequence of using small angle approximations for the attitude and surface gradient and retaining only the lead-order terms. For the same reason, (4) has no sensitivity to the spacecraft yaw angle. (See [29] for a detailed discussion.) The form arises because, to this level of approximation, the impulse response is not separately sensible to the pitch and roll angles and the surface gradient, but only to their relative orientation: rolling the space craft has the same effect on the echo shape as tilting the surface. The sensitivity of the echoes to the along-track slope is negligible, and we shall suppose generally that $\varsigma = 0$. This is not the case for the across-track slope, however, and we define the angle

$$\theta = \chi + \beta/\eta. \quad (9)$$

We term θ the 'interferometer angle'. For surfaces such as the ocean, this definition is consistent [28], with the geometric interpretation illustrated in the lower panel of fig. 1, namely that θ is the angle between the normal to the interferometer baseline and the direction of the point of closest range to the surface. With this definition, the dependence of the impulse response on the attitude becomes $X\left(\mu, \chi + \frac{\beta}{\eta}\right) \equiv X(\mu, \theta)$.

B. Small pitch angle form for the cross-product impulse response.

During nominal operation, the pitch and roll angles are small, of the order of 0.1° or less. However, as part of this study, we wish to apply the results to SARIN data acquired with larger roll angles, of the order of 1° . We therefore seek an expansion in small pitch angles of (4), to reduce the numerical complexity of the model of the cross-product, before proceeding to obtain expansions in small roll and pitch angle suitable for the SAR mode in the next section. The small pitch expansion is obtained by expanding the antenna gain in (4), and integrating term-by-term to obtain

$$\begin{aligned} & \int_0^{2\pi} d\vartheta d(\rho_k \cos\vartheta - \xi_k) e^{ik_0 B \rho_k \sin\vartheta} \\ & \quad \cdot \exp\left[-2\left(\frac{(\rho_k \cos\vartheta - \mu)^2}{\gamma_1^2} + \frac{(\rho_k \sin\vartheta - \theta)^2}{\gamma_2^2}\right)\right] \\ & \sim I_1(\rho_k; \theta, \xi_k) + \frac{4\rho_k \mu}{\gamma_1^2} I_2(\rho_k; \theta, \xi_k) + \\ & \quad \mu^2 \left(\frac{8\rho_k^2}{\gamma_1^4} I_3(\rho_k; \theta, \xi_k) - \frac{2}{\gamma_1^2} I_1(\rho_k; \theta, \xi_k) \right) \end{aligned} \quad (10)$$

to second order in the pitch, where

$$\begin{Bmatrix} I_1 \\ I_2 \\ I_3 \end{Bmatrix} = \int_0^{2\pi} d\vartheta \begin{Bmatrix} 1 \\ \cos\vartheta \\ \cos^2\vartheta \end{Bmatrix} d(\rho_k \cos\vartheta - \xi_k) e^{ik_0 B \rho_k \sin\vartheta} \cdot \exp \left[-\frac{2(\rho_k \sin\vartheta - \theta)^2}{\gamma_2^2} - \frac{2\rho_k^2 \cos^2\vartheta}{\gamma_1^2} \right] \quad (11)$$

Substituting (10) into (4) and performing the summation in (3), one arrives at

$$X(\tau, B) \sim \frac{\lambda^2 G_0^2 D_0 c \sigma^0}{32\pi^2 h^3 \eta} \cdot e^{-ik_0 B \theta} \left(\begin{array}{l} H_1(\tau; \theta) + \frac{\mu}{\gamma_1^2} H_2(\tau; \theta) + \\ \mu^2 \left(\frac{8}{\gamma_1^4} H_3(\tau; \theta) - \frac{2}{\gamma_1^2} H_1(\tau; \theta) \right) \end{array} \right) \quad (12)$$

where the definition of the functions in (12) is apparent from comparing their coefficients with the terms in (10).

C. Small pitch and roll angle forms for the SARIN mode, SAR mode and pulse-limited power impulse response.

In the SAR case, the baseline is zero. In addition, in the case of the ‘SAR’ measurements used here, the interferometer angle θ is also small. In this case, one can expand the impulse response in terms of θ too. One has in place of (10)

$$\begin{aligned} & \int_0^{2\pi} d\vartheta d(\rho_k \cos\vartheta - \xi_k) e^{-2\left(\frac{(\rho_k \cos\vartheta - \mu)^2}{\gamma_1^2} + \frac{(\rho_k \sin\vartheta - \theta)^2}{\gamma_2^2}\right)} \\ & \sim J_1(\rho_k; \xi_k) + \frac{4\rho_k \mu}{\gamma_1^2} J_2(\rho_k; \xi_k) \\ & \quad + \mu^2 \left(\frac{8\rho_k^2}{\gamma_1^4} J_3(\rho_k; \xi_k) - \frac{2}{\gamma_1^2} J_1(\rho_k; \xi_k) \right) \\ & \quad + \theta^2 \left(\frac{8\rho_k^2}{\gamma_2^4} J_4(\rho_k; \xi_k) - \frac{2}{\gamma_2^2} J_1(\rho_k; \xi_k) \right), \end{aligned} \quad (13)$$

where, now,

$$\begin{Bmatrix} J_1 \\ J_2 \\ J_3, J_4 \end{Bmatrix} = \int_0^{2\pi} d\vartheta \begin{Bmatrix} 1 \\ \cos\vartheta \\ \cos^2\vartheta, \sin^2\vartheta \end{Bmatrix} d(\rho_k \cos\vartheta - \xi_k) \cdot \exp \left[-2\rho_k^2 \left(\frac{\cos^2\vartheta}{\gamma_1^2} + \frac{\sin^2\vartheta}{\gamma_2^2} \right) \right] \quad (14)$$

In contrast to the pitch μ , (13) does not contain a linear term in the interferometer angle θ . This is natural, in that, if the satellite is pitched nose-up, for example, the forward-looking synthetic beams have an increased weighting from the antenna pattern, the backward beams a decreased weighting, and the reverse is true if the sign of the pitch changes. On the other hand, the echo shape in any particular beam is an even function with respect to the roll angle, that is, is insensitive to the sign of the roll.

On the other hand, one may use the symmetry properties of the integrands in (14) to show that

$$J_2(\rho_k; \xi_k) = -J_2(\rho_k; -\xi_k) . \quad (15)$$

If the summation in (3) is formed symmetrically with respect to forward and backward looking beams, as indeed it is written, the consequence of (15) is that there is no linear dependence on the pitch in the multi-looked echo. (If one wishes to measure the pitch, the behavior of individual beams is more sensitive than that of the multi-looked echo. [31] have used the distribution of power across the beams to determine the satellite pitch.)

In detail, for the measurements we use, the summation is not exactly symmetric with respect to the forward and backward beams, and at high values of altitude rate, there is a correction that is needed to account for this. However, none of the altitude rates encountered in this study are sufficient to warrant a correction. For completeness, the effect is described in Appendix C. In the remaining main text, we treat the summation as it appears in (3). Then, one has in place of (12),

$$\begin{aligned} X(\tau, 0) \sim & \frac{\lambda^2 G_0^2 D_0 c \sigma^0}{32\pi^2 h^3 \eta} \\ & \cdot \left(F_1(\tau) + \mu^2 \left(\frac{8}{\gamma_1^4} F_3(\tau) - \frac{2}{\gamma_1^2} F_1(\tau) \right) \right. \\ & \quad \left. + \theta^2 \left(\frac{8}{\gamma_2^4} F_4(\tau) - \frac{2}{\gamma_2^2} F_1(\tau) \right) \right) \end{aligned} \quad (16)$$

for the ‘SAR’ case, where the functions F are defined in the obvious way.

The pulse-limited case can be obtained in a similar fashion, by setting $D_0 = d \equiv 1$ and $\xi_k = 0$ in (4) which removes the synthetic beam formation and returns the problem to a pulse-limited geometry. One then has a form sufficiently similar to (16) that we do not give it separately. In the pulse-limited case, functions F in (15) can be given analytic form by expanding the impulse response of [19] (see also eqn. (36)) and allowing for Earth sphericity and the ellipticity of the antenna gain as has been done by [32]. In this work we have not made use of these expressions in that, having of necessity to compute (16) numerically in the SAR case, it is then simple (and introduces least possibility of error) to set $D_0 = d \equiv 1$ and $\xi_k = 0$ and re-compute the result.

D. The power and cross-product.

To determine the echo cross-product or power, the synthetic beams, the compressed pulse shape and the surface roughness density function need a definite form. We describe these in this subsection. The CryoSat-2 data that is available to us uses in ‘SARIN’ mode a Hamming weighting when forming its synthetic beams, and in consequence the synthetic beam pattern is

$$D_0 d(\phi) = \left(\sum_{n=0}^{N_a-1} \left(0.54 - 0.46 \cos \left(\frac{2\pi n}{N_a-1} - \pi \right) \right) e^{2ik_0 v_s \Delta t \phi \left(n - \frac{N_a-1}{2} \right)} \right)^2,$$

[(17)

On the other hand, the ‘SAR’ mode data uses a rectangular weighting, in which case

$$D_0 d(\phi) = \cot^2(\pi k_0 v_s \Delta_t \phi) \sin^2(N_a \pi k_0 v_s \Delta_t \phi). \quad (18)$$

In (17) and (18), ϕ denotes an angle measured from the maximum gain line of the beam. The compressed pulse of the SIRAL radar is accurately described by the function

$$p_t(\tau) = p_0 \operatorname{sinc}^2(\pi B_c \tau), \quad (19)$$

where B_c is the received bandwidth.

We use the Gaussian surface elevation density function given by

$$p_z(\tau) = \frac{1}{\sqrt{2\pi}\sigma} e^{-\frac{1}{2}(\tau/\sqrt{2}\sigma)^2}, \quad (20)$$

where $\sigma = 2\sigma_s/c$. (20) is an approximation to the actual distribution of the ocean surface. The ‘significant wave height’ (SWH) is equal to $4\sigma_s$. (It is possible, for example, extend (20) by a term that accounts for the skewness of the height distribution in the manner of [33]. In fact, we have investigated doing so. We found, however, that while the addition of a skewness term improved the least-square error of the fit, it significantly degraded the precision of the range measurement, and in most cases it was obvious even to the eye that the term was better fitting noise rather than better characterising the ocean surface. Therefore we have dropped this term in this paper.)

With the convolutions of (1) performed, one obtains in the SARIN case, for example,

$$\begin{aligned} \Psi_r(\tau, B) \sim & \frac{\lambda^2 G_0^2 D_0 c \sigma^0}{32\pi^2 h^3 \eta} e^{-ik_0 B \theta} \\ & \cdot \left(G_1(\tau; \theta, \sigma_s) + \frac{\mu}{\gamma_1^2} G_2(\tau; \theta, \sigma_s) \right. \\ & \left. + \mu^2 \left(\frac{8}{\gamma_1^4} G_3(\tau; \theta, \sigma_s) - \frac{2}{\gamma_1^2} G_1(\tau; \theta, \sigma_s) \right) \right) \end{aligned} \quad [(21)$$

where the definition of the functions G follow in the obvious way from (1) and (12). Similar, forms are obtained for the SAR and pulse-limited cases.

E. Effect of variations in satellite altitude and velocity.

Equation (20) and its analogous forms provide a description of the echo cross-product and power subject to small variations in the satellite pitch and, in the SAR and pulse-limited cases, roll. Two other system parameters also vary along the satellite orbit: the satellite altitude and satellite velocity. In this section we describe how these are accounted for.

The satellite altitude of CryoSat-2 varies over some 50 km around 730 km, and the power and cross-product have a first-order dependence on the altitude. While we have suppressed the dependence, the functions that appear in (21) are themselves functions of the altitude. The obvious approach to accounting for the variation is to return to (4), write $h = h_0 + \delta$ and seek an expansion of the integral in powers of the variation of altitude δ about the fixed altitude h_0 . This can be done in the pulse-limited case, but, in the ‘SARIN’ and ‘SAR’ cases, the integrand is singular as $h_0 + \delta \rightarrow -c\tau/(n\xi_k^2)$ as a result of (8), and its expansion does not converge there. However, this difficulty does not arise once the convolutions of (1) have been performed. Thus we obtain the leading order term in δ by determining the numerical derivative of, for example (21), with respect to δ . In fact, it is only the derivative of G_1 that is needed; the remaining terms are too small to need accounting. One then has

$$\begin{aligned} \Psi_r(\tau, B) \sim & \frac{\lambda^2 G_0^2 D_0 c \sigma^0}{32\pi^2 h^3 \eta} e^{-ik_0 B \theta} \\ & \cdot \left(G_1(\tau; \theta, \sigma_s) + \delta G_4(\tau; \theta, \sigma_s) + \frac{\mu}{\gamma_1^2} G_2(\tau; \theta, \sigma_s) \right. \\ & \left. + \mu^2 \left(\frac{8}{\gamma_1^4} G_3(\tau; \theta, \sigma_s) - \frac{2}{\gamma_1^2} G_1(\tau; \theta, \sigma_s) \right) \right) \end{aligned} \quad (22)$$

in place of (21), for example.

There are also small variations that occur through the dependence on height and velocity of the look angle sampling interval in (6) and the number of looks in (7). In fact, (6) and (7) give time averaged values, so that, for example, (7) does not generally provide an integer value for the number of looks N in SARIN and SAR modes. In detail, the number of looks is an integer that varies, by ± 1 , along the track in such a way as to provide the average value given by (7). However, the effect of the variations of these quantities on the echo impulse response is less than 0.25%, which is undetectably small, and we therefore ignore it.

There is also a separate effect that arises when the direction of the satellite velocity is not tangential to the surface at the nadir point. The look angles of the synthetic beams are formed relative to the normal to satellite velocity, and in the presence of an altitude rate, this results in an asymmetric distribution of beam look angles relative to the nadir direction, and in this case the summation of equation (3) is no longer symmetric about $k = 0$. However, the effect only becomes significant for high altitude rates, which were not experienced in the data acquisitions used in this study. For completeness, we give a more detailed description in Appendix C.

III. ECHO FLUCTUATIONS.

The echoes observed by the altimeter are subject to radar speckle and the purpose of the multi-looking is to reduce the fluctuations due to speckle. Even multi-looked, the echoes suffer a residual fluctuation, and this fluctuation is the main source of noise on the measurements of the ocean surface

parameters. A full description of the statistics of their residual fluctuation would require a fairly extensive Monte-Carlo approach, and we have not attempted this. However, in all cases the number of looks is fairly high, and in consequence the statistics of the multi-looked echoes are close to Gaussian. In consequence, the statistics are reasonably described once the variance of the multi-looked echoes is known, and it is the calculation of the variance and related quantities that is the main concern of this section. It is concluded with a comparison of the predicted fluctuation of the echoes with those observed in practice.

A. The effective number of looks.

Individual echoes ψ have real and imaginary parts that are Gaussian distributed. Using x^* to denote the conjugate of x , their power $p = \psi\psi^*$ is exponentially distributed [34]. An exponential distribution has the property that its variance equals the square of its mean. If N independent echo powers are averaged to form a multi-looked echo q , its variance is \bar{p}^2/N , where we use \bar{x} to denote the mean of x , or, alternatively, $N = \bar{p}^2/\sigma_q^2$ where we use σ_x^2 to denote the variance of x . In the present case, however, the echoes we deal with are, in general, correlated one with another, and, in addition, the mean echo varies from look-to-look. In consequence, the residual fluctuation is larger than one might suppose from simple considerations based on the number of looks N . We therefore follow [29] by introducing the effective number of looks, N_e , which is the number of looks that would give rise to the actual residual fluctuation had the multi-looked power been formed from independent echoes whose mean equals that of the multi-looked power.

In general let us denote a covariance function between two random variables a and b as C_{ab} and associate with it a correlation coefficient $R_{ab} = C_{ab}/\sigma_a\sigma_b$. Let ψ denote an individual echo and let $p = \psi\psi^*$ denote the echo power. All the echoes we deal with are incoherent, that is, their mean $\bar{\psi} = 0$. In consequence their variance $\sigma_\psi^2 = \overline{\psi\psi^*} - \bar{\psi}\overline{\psi^*} = \overline{\psi\psi^*} = \bar{p}$, that is, their variance equals the mean power. Let $t = \psi_1\psi_2^*$ be the cross-product between two incoherent echoes ψ_1 and ψ_2 with equal mean powers \bar{p} . The covariance between the two echoes is then $C_{\psi_1\psi_2} = \overline{\psi_1\psi_2^*} - \bar{\psi}_1\bar{\psi}_2^* = \overline{\psi_1\psi_2^*} = \bar{t}$, and

$$R_{\psi_1\psi_2} = \bar{t}/\bar{p} \quad (23)$$

in this case. In this context the correlation coefficient is usually termed the *coherence* of the two echoes. t has the probability density function [25]

$$p_{\psi_1\psi_2}(z) dz = \frac{2}{\pi\bar{p}^2(1-R_{\psi_1\psi_2}^2)} K_0\left(\frac{2|z|}{\bar{p}(1-R_{\psi_1\psi_2}^2)}\right) \exp\left(\frac{2R_{\psi_1\psi_2}\mathcal{R}(z)}{\bar{p}(1-R_{\psi_1\psi_2}^2)}\right) \quad (24)$$

Here, $\mathcal{R}(z)$ describes the real part of z . From this density function, one may obtain the result $\overline{tt^*} = \bar{p}^2(1+R_{\psi_1\psi_2}^2)$. One thus has $\sigma_t^2 = \overline{tt^*} - \bar{t}\bar{t^*} = \bar{p}^2$, that is, the variance of the cross-product is simply the square of the mean power. However, since $\overline{tt^*} = \overline{\psi_1\psi_2^*\psi_2\psi_1^*} = \overline{\psi_1\psi_1^*\psi_2\psi_2^*} = \bar{p}_1\bar{p}_2$, one also has

$$C_{p_1p_2} = \overline{p_1p_2} - \bar{p}^2 = \bar{p}^2 R_{\psi_1\psi_2}^2 = C_{\psi_1\psi_2}^2 \quad (25)$$

This is an extremely useful result, in that it permits us to determine the covariance of the power in terms of the covariance of the field. (This result is not original; it appears, for example, in a rather more general setting, in [35].)

In the event that $\psi_1 = \psi_2$, $t = p$, $R_{\psi_1\psi_2} = 1$, (21) reverts to the familiar exponential distribution for the power of an incoherent echo, and (25) simply expresses the familiar result that the variance of the power equals the mean power squared. (It is interesting to note, as we do following (24), that this result holds in the more general case of a partially coherent cross-product.)

Let the multi-looked cross-product or power be the sum of N individual looks $q = (1/N)\sum_{n=0}^{N-1} t_n$, where t_n denotes an individual look. We define the effective number of looks to be $N_e = \overline{qq^*}/\sigma_q^2$. Then

$$\begin{aligned} \sigma_q^2 &= \overline{(q - \bar{q})^2} = \frac{1}{N^2} \sum_{n=0}^{N-1} \sum_{m=0}^{N-1} \overline{(t_n - \bar{t}_n)(t_m - \bar{t}_m)} \\ &= \frac{1}{N^2} \sum_{n=0}^{N-1} \sum_{m=0}^{N-1} \overline{p_n} \overline{p_m} R_{t_nt_m} , \end{aligned} \quad (26)$$

and thus, in general, that

$$N_e = \frac{|\sum_{m=0}^{N-1} \bar{t}_m|^2}{\sum_{n=0}^{N-1} \sum_{m=0}^{N-1} \overline{p_n} \overline{p_m} R_{t_nt_m}} . \quad (27)$$

In the event that we are concerned with multi-looked powers, rather than the cross-product, one has $\bar{t}_n \bar{t}_m^* = \overline{p_n} \overline{p_m}$ in the denominator on the right-hand-side (RHS) of (27). From (27) one has in general that $N_e \leq N$.

In the following subsections, the statistics of the echoes in the SAR, SARIN and pulse-limited cases is considered separately to arrive at simpler representations in each of these cases.

B. Independence of the looks in SAR mode.

In the SAR case, we are dealing only with powers, and the mean powers $\overline{p_n}$ that then appear in the denominator and numerator of (27) are those obtained by applying (1) to the individual impulse responses of (4). The correlation coefficient in (27) is then the correlation that occurs between different look angles. In the L1b processor, each look comes from a different burst, and the principle mechanism that gives rise to decorrelation is the spatial fading that arises from the displacement of the antenna between looks. At least for neighbouring looks, the change in angle between looks is very small and has little effect on the echo power, and the look

angle is adjusted so that each look illuminates the same area of surface. The decorrelation can then be examined by considering the covariance between the echo at a given look-angle and that which would be observed when the antenna is displaced along-track by a small horizontal distance x , that is, we consider the covariance function $C_k(\tau, x)$, where k denotes the look angle through (6).

In this case the covariance can be obtained by following a similar path as [29] (see also [36]). $C_k(\tau, x)$ is given by a similar triple convolution to (1), namely,

$$C_k(\tau, x) = p_t(\tau) * p_z(\tau) * \Pi_k(\tau, x) , \quad (28)$$

here, in this case, the covariance impulse response is given by

$$\begin{aligned} \Pi_k(\tau, \xi_k, x) \sim & \frac{\lambda^2 G_0^2 D_0 c \sigma^0}{32\pi^2 h^3 \eta} H\left(\tau + \frac{\eta h \xi_k^2}{c}\right) \\ & \cdot \int_0^{2\pi} d\vartheta d(\rho_k \cos\vartheta - \xi_k) e^{2ik_0 x \cos\vartheta} \\ & \cdot \exp\left[-2\rho_k^2 \left(\frac{\cos^2\vartheta}{\gamma_1^2} + \frac{\sin^2\vartheta}{\gamma_2^2}\right)\right] \end{aligned} \quad (29)$$

It may be noted that the expression for Π_k is essentially the same as that of X_k , save that the phase difference in (4) that arises between the two antennas displaced across-track is replaced in (29) with the phase difference that occurs between the same antenna at two different locations along the track, and a factor of 2 appears because, unlike the interferometer, path differences occur on transmission and reception. In (29) we have also assumed nadir antenna pointing, ignoring the small effect of pitch and roll on the covariance function.

With the covariance obtained from (28) and (29), and the power of an individual look obtained from (1) using (4) with $B = 0$, the correlation function may be computed. In fig. 2 we show the power correlation coefficient for various look angles at $\tau = \eta h \xi_k^2 / c$ as a function of the along-track separation x . (The numerical values we have used in this and future calculations are given in Table B.1 of Appendix B). The upper panel of fig. 2 shows the correlation functions at zero SWH; the lower panel of fig. 2 shows the correlation functions with a SWH of 4 m. At low wave heights and small look angles, the power de-correlates over some 20 m. This is the expected result for a beam-limited system, in that the de-correlation distance is approximately equal to the aperture length, which in this case is 26 m. At higher look angles, however, the beams become pulse-limited along-track, and the de-correlation length correspondingly increases.

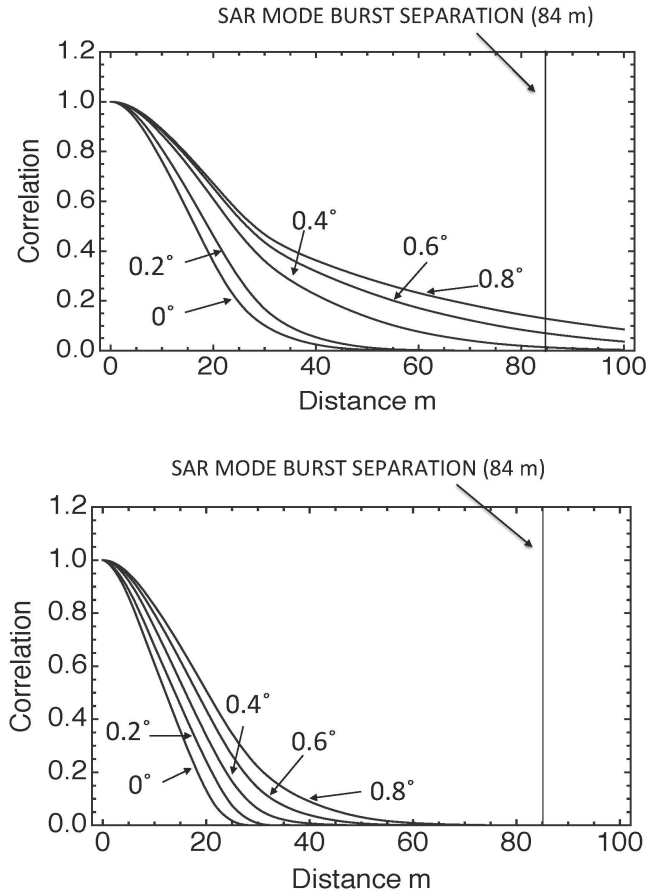


Fig. 2. Power correlation coefficient for a sequence of look angles as a function of the along track separation of the looks at (upper panel) zero wave height, and (lower panel) 4 m wave height. Also shown is the along track separation of the bursts in SAR mode of 84 m. In SARIN mode, the burst separation is 336 m.

Marked on the figures in fig. 2 is the spatial separation of the bursts in SAR mode, 84 m. It can be seen that at this separation, most of the beams at zero wave height will have de-correlated, although some correlation remains at high look angles. With appreciable wave height, however, all of the beams de-correlate, exhibiting a beam-limited behaviour. This occurs because the effect of the wave height is to extend the pulse-limited area to the extent that the synthetic beams are become beam, and not pulse, limited in the along-track direction. However, even when the wave height is low, the beams that remain correlated have very little weight in the multi-looking, because they are heavily weighted by the antenna pattern.

Thus, in practice, it is a good approximation to assume that the looks are independent in SAR mode. One therefore has $R_{t_n t_m} = \delta_{m,n}$ and (27) simplifies to

$$N_e^{(S)} = \frac{\left| \sum_{m=0}^{N_S-1} \bar{p}_m \right|^2}{\sum_{m=0}^{N_S-1} \bar{p}_m^2} \quad (30)$$

in SAR mode.

C. Correlation between the powers at the interferometer antennas and the coherence of the echo cross-product.

In SARIN mode, the burst separation is larger than in the SAR mode, some 336 m, and the conclusion that the echoes in each beam are uncorrelated one from another carries over from the SAR mode. In the case of the echo cross-product, one then has

$$N_e^{(SIC)} = \frac{\left| \sum_{m=0}^{N_{SI}-1} \bar{p}_m R_{LR}(m) \right|^2}{\sum_{m=0}^{N_{SI}-1} \bar{p}_m^2} \quad (31)$$

where we have made use of (23), and we denote by $R_{LR}(m)$ the correlation, or coherence, between the cross-product of the echoes at the left and right antennas (see fig. 1).

If, on the other hand, we consider the echo power in the SARIN mode, determined by summing the power over the beams, as is the case for SAR mode, at each antenna, and then summing the result for each antenna,

$$N_e^{(SIP)} = \frac{2 \left| \sum_{m=0}^{N_{SI}-1} \bar{p}_m \right|^2}{\sum_{m=0}^{N_{SI}-1} \bar{p}_m^2 (1 + R_{LR}^2(m))}, \quad (32)$$

where we have made use of (25) to express the correlation between the echo powers at the two antennas in terms of the coherence of their fields. The number of looks, $2N_{SI}$, is doubled when using the SARIN echo power because the measurements at both antennas are incoherently summed. Thus the same correlation function appears in both the expressions for the multi-looked cross-product, and the multi-looked power, but with opposite effect: a high correlation results in a high number of effectively independent looks in the case of the cross-product, but has the effect of reducing the number of effectively independent looks in the case of the multi-looked power.

In this case, the covariance function impulse response is that of the echoes arriving at the right and left antennas. The corresponding covariance impulse response is simply that of (4), and the power impulse response also given by (4) with $B = 0$. Fig. 3 shows the power correlation function of the echoes at the two antennas at two look angles as a function of echo delay time $\tau + \eta h \xi_k^2 / c$. The upper panel of fig. 3 shows the coherence for zero wave height; the lower panel of fig. 3 the coherence at 4 m wave height. It can be seen that at zero echo delay, the correlation remains high in all cases. Even at high wave heights the correlation exceeds 0.7, while for small wave heights and beam look angles, the correlation is close to one. Since the height precision is most sensitive to the echo in the vicinity of zero delay time, it is apparent that summing the echo powers from the two antennas will not provide much improvement in the height precision over that obtained from an echo from a single antenna.

Except for negative delays, the correlation is only weakly dependent on the look angle, and at negative delays the differences are those occurring at very low signal powers, where, in practice noise and other small instrumental

disturbances occur. (The oscillatory character of the 0° look angle plot in the zero wave height case in the upper panel of fig. 3 is the result of the single point target impulse response in (19). For other values of look angle or wave height these are smoothed out either by the spreading in delay time of the echo, or the wave height distribution.) Thus one can make the reasonable approximation to the effective number of looks of (32) that, for the SARIN mode multi-looked power

$$N_e^{(SIP)} = \frac{2 \left| \sum_{m=0}^{N_{SI}-1} \bar{p}_m \right|^2}{(1 + R_{LR}^2(0)) \sum_{m=0}^{N_{SI}-1} \bar{p}_m^2}. \quad (33)$$

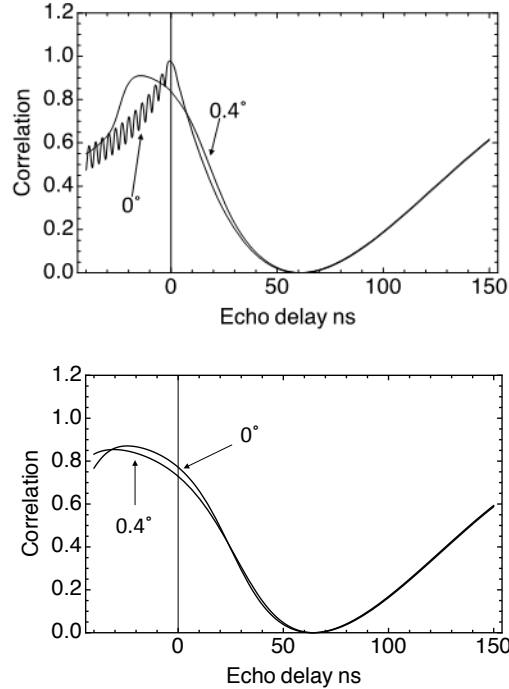


Fig. 3. Power correlation coefficient between the echoes at the two antennas of the interferometer for two looks angles at (upper panel) zero SWH, and (lower panel) 4 m SWH. Note that the power correlation coefficient is the square of the modulus of the coherence. The oscillatory character of the 0° incidence beam at zero SWH is the result of the single point target response; at higher SWH or look angles this oscillation is washed out by the convolution of (1).

The correlation functions in fig. 3 also have a separate relevance in that they are the square of the coherence of the beam cross-product, and, in this case a high coherence results in a large effective number of looks. From fig. 3 one can see that the effective number of looks will be high in the vicinity of zero delay time, but will fall as the delay-time increases. We shall find this reduction in the effective number of looks apparent in the measured cross-product phase noise.

D. Correlation between the powers of the pulse-limited looks.

In contrast to the SARIN mode and SAR mode cases, the multi-looking of the pulse-limited echoes sums over echoes

drawn from the same mean, so that $\bar{p}_n = \bar{p}_m$ in (27), which in consequence simplifies to

$$N_e^{(PL)} = \frac{N_p^2}{\sum_{n=0}^{N_p-1} \sum_{m=0}^{N_p-1} R_{pnpm}} . \quad (34)$$

In this case, $N_e^{(PL)} < N_p$ if the individual looks are correlated one with another.

In the pulse-limited case, the corresponding covariance function is again that resulting between two echoes observed with a small along-track displacement x . As is the case for the pulse-limited power, one may obtain this covariance function by setting $D_0 = d \equiv 1$ and $\xi_k = 0$ in (29) to obtain

$$\Pi(\tau, x) \sim \frac{\lambda^2 G_0^2 c \sigma^0}{32\pi^2 h^3 \eta} H(\tau) \\ \cdot \int_0^{2\pi} d\theta e^{2ik_0 x \cos \theta} \exp \left[-2 \left(\frac{c\tau}{h\eta} \right) \left(\frac{\cos^2 \theta}{\gamma_1^2} + \frac{\sin^2 \theta}{\gamma_2^2} \right) \right] \quad (35)$$

for the covariance impulse response. (For small ellipticity, following the method of [32] this integral can be given the approximate form

$$\Pi(\tau, x) \sim \frac{\lambda^2 G_0^2 \sigma^0 c}{16\pi h^3 \eta} e^{-\left(\frac{2c\tau}{h\eta\bar{\gamma}^2}\right)} J_0 \left(2k_0 x \sqrt{\frac{c\tau}{h\eta}} \right) \quad (36)$$

where J_0 denotes a Bessel function of the first kind, and $2/\bar{\gamma}^2 = 1/\gamma_1^2 + 1/\gamma_2^2$. If one ignores the ellipticity, (36) is the result of [36]. If one sets $x = 0$ in (36) one obtains the pulse-limited power impulse response. (36) is [19] expression for the impulse response, allowing for the sphericity of the Earth and the small ellipticity of the antennas [32]. (While we have used a numerical integration of (35) to obtain the results in this section, we have used (36) to verify the numerical integrations.)

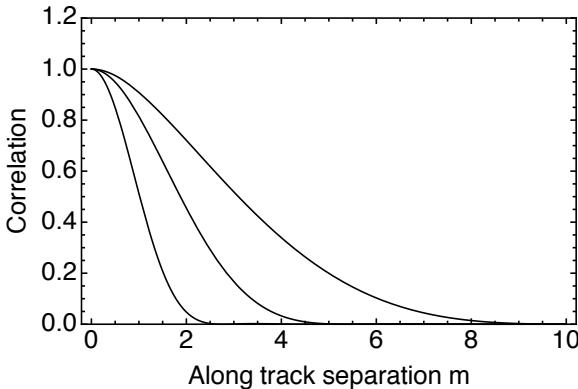


Fig. 4. Power correlation coefficient of the pulse-limited echoes at zero delay time for wave heights of 0 m, 2 m and 4 m, as functions of the along track separation of the echoes. Increasing wave height corresponds to more rapid de-correlation. When pulse-limited echoes are formed from SAR mode operation, the separation of the echoes is 0.41 m.

Fig. 4 shows the power correlation coefficient for the pulse-limited echoes at zero delay time and for three different wave

heights. In a burst, the echoes are separated along-track by 0.41 m. It can be seen that at all wave heights, successive echoes in the burst are highly correlated, and even at high wave heights, only every 5th echo is completely de-correlated at zero echo delay. The rates of decorrelation in Fig. 4 are in qualitative agreement with those suggested previously by a more approximate argument [37], [38].

E. Comparison of the predicted and measured effective number of looks.

We close this section with a comparison of the calculated effective number of looks N_e for the SARIN mode cross-product, the SAR mode power and the pulse-limited power. (The results for the SARIN mode power are essentially the same as those of the SAR mode.) A description of what determines the number of looks in each mode, and how the multi-looking is performed in practice in the three cases is given in appendix A. In the following we make comparisons of echoes at the 20 Hz rate, which is the highest rate at which echoes are available in all three data sets.

Fig. 5 shows a comparison between the effective number of looks $N_e^{(SIC)}$ of the SARIN echo cross-product calculated from (31) with the observed value at the 20 Hz rate. It can be seen immediately that the effective number of looks $N_e^{(SIC)}$ is considerably smaller than the actual number of looks N_{SI} : for positive delay times, both the calculated and the observed effective number of looks is less than half the actual number of looks, which is 63 in this case. This is the result of forming multi-looked echoes drawn from populations with different means. Because some echoes have a higher power than others, so too do their speckle fluctuations, and in consequence they have greater weight in the summation than would be the case if all the echoes were of equal power [29].

The behavior of the effective number of looks as a function of delay time, however, is dominated by the variation of the correlation function, as a comparison of fig. 5 with fig. 3 demonstrates. While the maximum effective number of looks occurs around zero delay time, it falls rapidly towards zero at around 60 ns. The speckle suppression of the multi-looking is poor at larger delay times. This is apparent in the noticeable increase in phase noise that is visible in the observations, as illustrated in fig. B1.

There is a less agreement between prediction and observation at zero delay times, and at larger negative delays, although the causes of these are different. Firstly, the theory in this section supposes that speckle noise is the only source of fluctuation. If there is a source of variation in the observations in addition to that due to speckle, the observed effective number of looks will be less than predicted. In particular, the echoes are very sensitive to the surface roughness in the vicinity of zero delay time. We formed the observed values of the effective number of looks by examining the along-track variances (the details are provided in appendix B), and in consequence the observations include whatever variations result from changes in the roughness along the track, whereas the theory has been evaluated at a fixed roughness. There is

additional variability in the data that is not present in the theory, and some difference between the two in the vicinity of zero delay is to be expected.

At larger negative delay times, the observations show greater variability than is predicted theoretically. We have not been able to identify precisely the source of this behavior, but, for these values of delay time, the echo power is very small, and the estimate of the effective number of looks is the ratio of two very small numbers (the mean echo squared and the variance of the echo). Small errors in the theory arising from approximations used to obtain (4), for example, or small departures of the actual instrument from its theoretical description, will result in significant differences in the comparison of theory with observations. However, because the echo powers are small, this behavior has little effect on the measurement precision of the parameters.

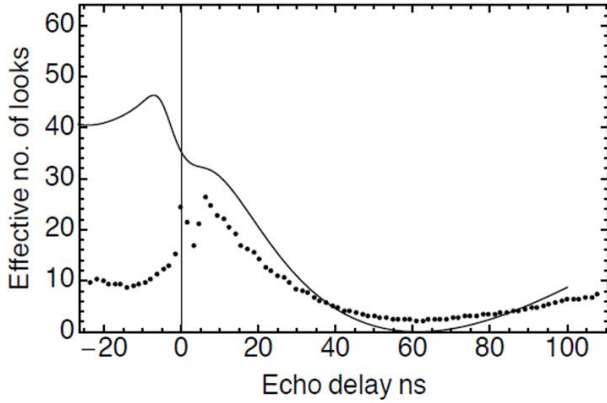


Fig. 5. Comparison of the calculated (solid line) and observed (dots) effective number of looks at 20 Hz of SARIN mode echo cross-products. The calculated curve is for a wave height of 2 m. The actual number of looks at 20 Hz is 61.

Turning to the case of the SAR echo power, fig. 6 shows the corresponding comparison in this case, where the calculated values use (30). As argued in section III(B), the echoes that contribute to the multi-looked echo are independent; the difference between the actual and effective number of looks is, in theory, entirely the result of forming the looks from different statistical populations. Because all the looks are independent, there is a somewhat higher ratio of effective to actual looks, or around 180:204 in this case. In practice, the effective number of looks is somewhat smaller, around 140 looks, and, as with the SARIN cross-products, the echoes in the vicinity of zero delay time have greater variability than the theory acknowledges.

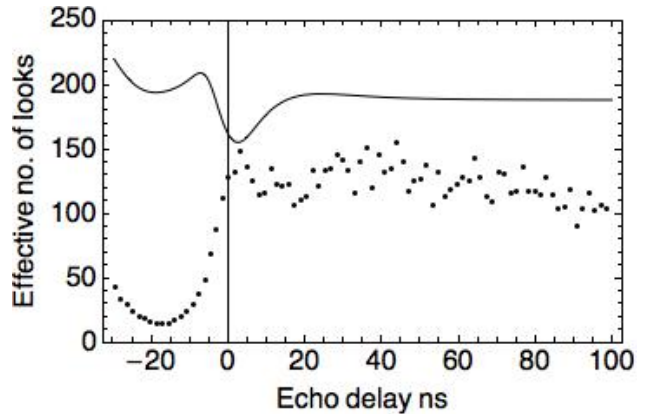


Fig. 6. Comparison of the calculated (solid line) and observed (dots) effective number of looks at 20 Hz of SAR mode echoes. The calculated curve is for a wave height of 2 m. The actual number of looks at 20 Hz is 240.

In the case of the pulse-limited observations, fig. 7 shows the comparison of the effective number of looks of the pulse-limited echoes where the theoretical values are calculated from (34). In contrast to the SAR echoes, the pulse-limited echoes are drawn from the same statistical population, and the disparity between the actual and effective number of looks is entirely the result of correlations between the looks. Fig. 4 illustrates that at zero delay-time, approximately only every fifth of the pulse-limited echoes can be considered independent at high wave-heights, and this is apparent too from the ratio between the actual and effective number of looks illustrated in fig. 7, in which the ratio is closer to 1:6. The effective number of looks improves at higher delay times, due to the greater spatial distances between the area illuminated at a given delay-time.

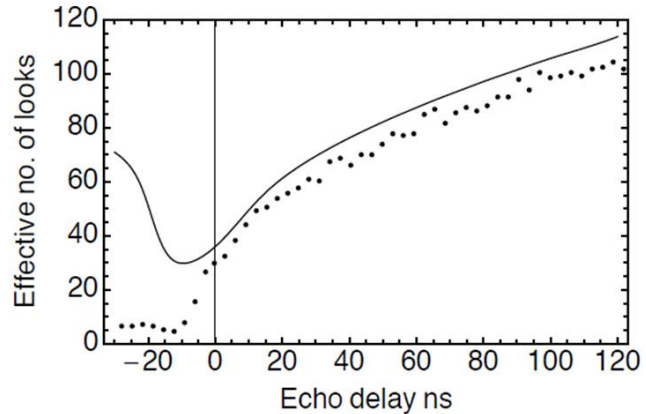


Fig. 7. Comparison of the calculated (solid line) and observed (dots) effective number of looks at 20 Hz of pulse-limited echoes observed in SAR mode. The calculated curve is for a wave height of 2 m. The actual number of looks at 20 Hz is 256.

Overall, however, the comparison between the actual and effective number of looks is reasonably close. Even in the case of the SAR mode echo powers, the ratio between the theoretical and measured number of looks is approximately 5:4. Thus, one may conclude that during its operation, the CryoSat-2 SIRAL radar is operating close to its theoretical

limit in achieving speckle suppression.

IV. APPLICATIONS TO PRECISE MEASUREMENTS OF THE OCEAN SURFACE.

In this section we apply the models of section II to the observations of the SARIN mode cross-product and SAR mode and pulse-limited echo powers to examine the accuracy and the precision of the ocean surface parameters that may be obtained from CryoSat-2 echoes. Appendix A contains a detailed description of the data acquisitions that were used in this section, and how the SARIN, SAR and pulse-limited echoes are formed from these acquisitions; appendix B contains details of the model calculation and fitting, and post-processing that we applied to the data to obtain the results.

A. Unbiased measurement of the interferometer angle.

The interferometer of CryoSat-2 is designed to measure the across-track slope of the surface by subtracting the roll angle χ from the measured interferometer angle θ using (9) and as illustrated in fig. 1. The measurement of across-track slope has been the subject of a detailed calibration over the ocean [28] that made use of accuracy with which the across-track slope of the ocean surface is now known [39]. The interferometer angle is defined as that associated with the echo from the point on the surface closest to the interferometer (see fig. 1), and in this calibration, the interferometer angle was measured by associating with it the phase of the echo cross-product at the time of first-arrival. This method is a necessary one if the interferometer is to be used over ice sheet surfaces, whose detailed geometry is unknown, and it is for this reason that the calibration was performed that way.

A consequence of working this way is that the measurements of the interferometer angle that results are biased. The bias is a consequence of the finite width of the transmitted pulse, the surface roughness, and the finite resolution of the synthetic beams in the along-track direction, the point of closest approach cannot be uniquely associated with the cross-product phase at a particular arrival time; if it is, as this method assumes, the resulting measurement of the interferometer angle contains a bias that is a function of the roll angle and the surface roughness. This is illustrated in the upper panel of fig. 8, which shows a regression between the calibration error, that is, the error in the value of the measured across-track ocean surface slope, and the measured value of θ , for a suite of SARIN observations of the Pacific and Indian Oceans.

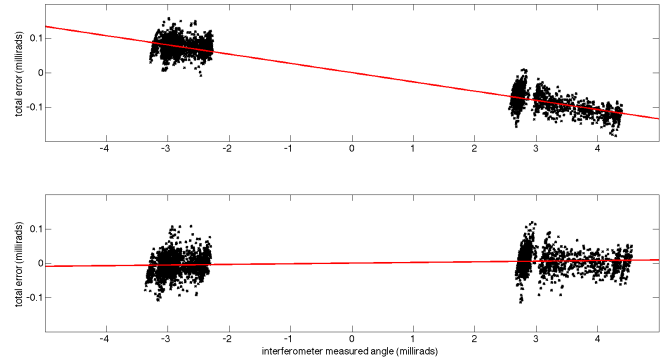


Fig. 8. The error in the measurement of across-track slope when (upper panel) the phase of the SARIN echo cross-product at the time of its first arrival is used to determine the interferometer angle θ ; and (lower panel) when the echo cross-product is fitted with the model of (22), together with their best-fitting regression lines. While the regression line in the lower panel has an observable gradient, it is not statistically significantly different from zero.

The functional dependence of the bias on θ and σ_s is theoretically predictable and can be removed as a post-measurement correction. (In the case of θ , the dependence is a linear one, as the upper panel of fig. 8 shows.) Nonetheless, as [28] point out, over surfaces of known geometry such as the ocean, the entire phase history of the cross-product is uniquely dependent on θ . Fitting the cross-product with an accurate model should remove these biases. In the lower panel of fig. 8, the result of repeating the calibration is shown, save that, in this case we have fit the model of (22) to determine the angle θ . (An example of such a fit is shown in fig. B1.) The fitting has removed the roll dependent bias, as is apparent from the lower panel of fig. 8, and (not shown) the surface roughness dependent bias too. Fitting with an accurate model results in an unbiased measurement of the across-track slope, at least to the accuracy with which a calibration can be performed.

We conclude this section by comparing the precision of the measurements of the interferometer angle when either picking the first arrival phase from the SARIN echo cross-product, or from fitting the model of (22) to the cross-product. Fig. 9 shows the distributions of the estimates of the interferometer angles for the two cases (with the bias removed in the former case). One can see that the fitting sacrifices some precision. While, in contrast to picking the first arrival phase, the fitting employs the entire echo (illustrated in fig. B1), the decrease in coherence with delay time results in the additional samples available to the fit having little impact on the precision of the measurement.

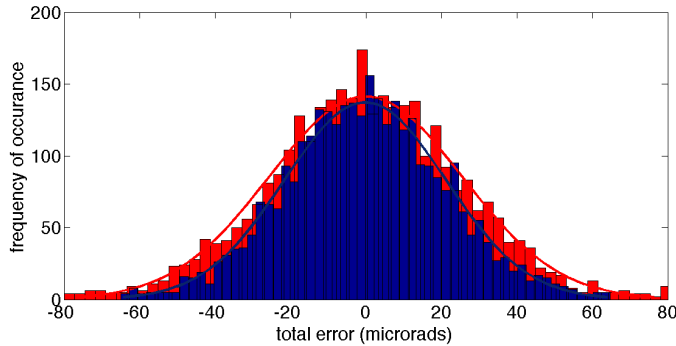


Fig. 9. The distributions of the error in interferometer angle as derived from (blue) picking the first-arrival phase of the echo cross-product, and (red) retrieved from fitting (22) to the cross-product. The blue and red distributions have standard deviations of 21.4 and 25.5 micro radians respectively, illustrating that some measurement precision is sacrificed in obtaining unbiased measurements.

B. Equivalence of SAR and pulse-limited echo measurements.

The use of a SAR mode offers potential advantages in precision over that of conventional pulse-limited altimetry (which are examined in the next section). Nonetheless, the question arises as to whether its use would introduce biases in operational ocean forecasts that presently make use of pulse-limited altimeter observations. We examine this question in this section.

While in principle it should be possible to derive unbiased estimates of the ocean surface parameters independently of the mode of altimeter operation, in practice biases emerge for two reasons: because of approximations made in the model of the echo from the altimeter, or because of imperfections in the operation of the instrument. Obtaining unbiased estimates requires a close correspondence between the theoretical description of the measurement, the actual operation of the instrument, and the scattering behavior of the surface. Determining the absolute biases in the derived parameters is also practically difficult: it demands that other, independent measurements of a greater accuracy are available with which to determine the bias, and, except in the case of averages over large space and timescales, this presents considerable difficulty. On the other hand, there are considerable geometric differences between pulse-limited and SAR mode operation. Their different effect on the echo make a demand that parameter estimates made at the same ocean location at the same time by the two modes show no bias in their difference, a fairly stringent requirement. It is unlikely that model approximation or instrument imperfections will affect the two measurements in the same fashion or to the same degree.

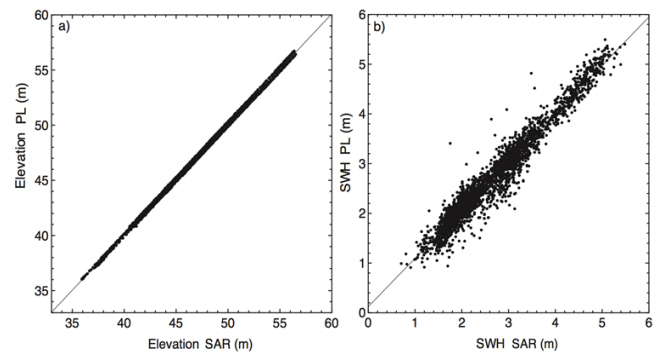


Fig. 10. A comparison between the measurements of: (a) sea surface elevation above the ellipsoid, and (b) significant wave height, obtained from SAR mode and pulse-limited echoes at the same location and time west of Portugal in the North Atlantic from 4th to the 9th January 2011. The best fit lines which are superimposed on the observations are in case (a) $y = 1.002 x + 0.009$, and in case (b) $y = 0.971 x + 0.149$. In neither case is the difference of the gradient from unity statistically significant.

As the synthetic aperture of the SIRAL altimeter is formed from data that are already telemetered to ground, it is possible to make a direct comparison between the parameters determined from echoes formed with and without the synthetic aperture. Fig. 10 compares the elevation and SWH measurements obtained from observations in SAR mode, processed as pulse-limited and SAR mode echoes, obtained from observations of the North Atlantic west of Portugal in the period 4th to the 29th January 2011. (The data themselves, and the detailed processing used to obtain these results, is described in appendices A and B.) The figure shows that, over a wide range of sea state conditions (the wave heights range from 0.8 to 5.5 m), we were not able to detect a significant bias between the pulse-limited and SAR mode measurements. Fig. 10 shows a comparison between some 6000 individual measurements over a total of some 3500 km of satellite track. One can have confidence that, were in future SAR observations to be preferred over those of pulse-limited geometry, it would be possible to maintain continuity with earlier missions in supplying measurements to operational forecast models.

C. Precision of SAR and pulse-limited measurements.

In any simple instrument, of which a mercury thermometer might be taken as an archetype, there is a relationship between the quantity that is measured, and that which is wanted: length and temperature being the two quantities in the case of a thermometer. In an altimeter range measurement, the corresponding quantities are power and range, and the precision of the range measurement can be simply represented by the equation

$$\Delta r = \frac{dr}{dp} \Delta p \quad (37)$$

where dp/dr is the sensitivity of the measurement and Δp and Δr are the precision of the power and range measurements. While an exact interpretation of (37) in the case of an altimeter measurement is somewhat involved, a simple interpretation

provides nonetheless a very useful framework with which to discuss the precision of the SAR and pulse-limited modes of operation.

The sensitivity is primarily determined by the gradient of the leading edge of the echo: the steeper the leading edge, the more sensitive the range measurement. Thus, the reciprocal of the sensitivity will depend on the surface roughness σ_s . On the other hand, the precision of the power determined by the fitting depends on the reciprocal of the square root of the number of statistically independent samples that are used in the fit in the vicinity of the leading edge, and this will vary as $\sigma_s^{-1/2}$. The two effects together result in a square root dependence of the precision on the surface roughness, that is

$$\Delta r \propto (\sigma_s) \sigma_s^{-\frac{1}{2}} = \sigma_s^{\frac{1}{2}}. \quad (38)$$

This slow increase (that is, worsening) in precision is apparent in all altimeter measurements of range. Fig. 11 shows the precisions we have obtained from fitting the SAR mode and pulse-limited mode echoes, and this slow dependence on the wave-height is apparent in both sets of data. At small roughness, the precision is limited by the pulse-width, which is why the curves do not pass through the origin as (38) would suggest, but the behaviour is clear at higher roughness.

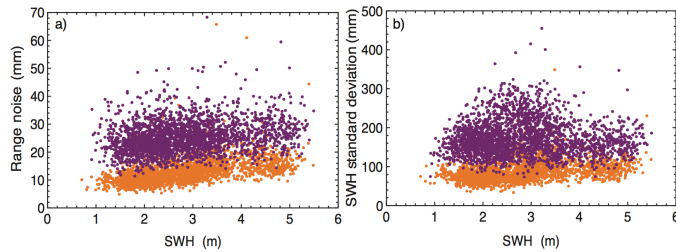


Fig.11. A comparison of the precision of SAR mode (orange) and pulse-limited measurements (magenta) of (a) the range measurement, and (b) the significant wave-height measurements obtained from 1 month of observation of the north west Atlantic Ocean in January 2011.

In an altimeter measurement of range, where one wishes to make the precision of the measurement as small (that is, good) as possible, there are, essentially, two ways to achieve this. One can either seek to maximise the sensitivity, or reduce the power precision, or both. With regard to the sensitivity, SAR mode operation offers an advantage, because its narrower impulse response (described in detail in [29]) results in a steeper leading edge slope than does the pulse limited mode for a given surface roughness. [26] first drew attention to the change of leading edge slope which results from using along-track aperture synthesis, although the description of the leading edge used there is not that which occurs in practice, and the spreading in range of the off nadir beams from which the echo is formed reduces the sensitivity gain that would result were only the nadir beam employed.

The second approach is to improve the power precision by increasing the effective number of looks. In fact, the 'factor of 2' with which the SAR and pulse-limited mode precisions differ in fig. 11 is not a result of differing sensitivity but the

difference in the effective number of looks. As figs. 6 and 7 show, these are very different for the two data, because the SAR mode PRF is determined by the need to prevent aliasing of the synthetic aperture, and not, as in conventional pulse-limited altimetry, to de-correlate the pulse-limited echoes. The difference between the two data sets of fig. 11 is no more than a coincidental consequence of the burst timing of the SIRAL SAR mode; it is not in any sense an intrinsic feature of the two modes.

Indeed, one may predict from the results of fig. 11 that the LRM mode of the SIRAL altimeter will match that of the SAR mode illustrated in fig. 11. This has a conventional, pulse-limited timing arrangement with a PRF of 1971 Hz [23]. This corresponds to a separation between the pulses of 3.8 m, which, as fig. 4 shows, will result in all but the lowest wave heights of each pulse providing an independent look. At a 20 Hz rate, the LRM mode will provide an effective 99 looks at zero delay time as opposed (see fig. 7) to the 35 that provides the precision illustrated in fig. 11. Thus one may anticipate an improvement in the LRM mode over that of fig. 11 of $\sqrt{99/35} = 1.68$, *i.e.*, a precision similar to that of the SAR mode, and indeed a precision of 13 mm in LRM mode has been reported [40].

[27] have argued that SAR altimetry offers an advantage over that of pulse-limited altimetry in that it provides a greater degree of incoherent integration, that is, a higher number of looks. In fact, the number of looks provided by SIRAL, 5480 per second, is larger than the 5120 considered by them, and, as section III(E) demonstrates, the performance of SIRAL is close to the theoretical limit imposed by speckle fluctuation, and yet the performance of the SAR and LRM modes is very similar. The combination of the actual sensitivity and effective, rather than actual, number of looks that occur in practice does not produce a superior precision in the SAR case.

This is not to argue that a SAR altimeter offers no improvement over a pulse-limited mode of operation at a similar carrier frequency. The SIRAL radar was not designed to maximize the number of looks, and the limited cost of its development depended considerably on the heritage of the Poseidon altimeter development, and particularly its internal timing. However, as [30] has observed, the introduction of an open burst configuration, and taking advantage of the known geometric form of the ocean surface, may allow an increase in the number of looks over that of the SIRAL design.

There is in fact an interesting trade off that has yet to be investigated. In this paper, we have not introduced any weighting into the summation of the beams in (3). If, on the one hand, one were to give weight to only the central beams, which suffer less from spreading in range, one will increase the sensitivity in (37), and in addition, as fig. 3 shows, the beams will, largely, de-correlate over a single aperture length. On the other hand, if one gave greater weight to the beams that lie further from nadir, one would increase the effective number of looks and thus reduce the power precision, although their de-correlation will occur at larger aperture separations. To the authors' knowledge, this trade off, and

hence the ultimate sensitivity of SAR mode echoes, has yet to be determined.

APPENDIX A. THE CRYOSAT-2 DATA.

In this study, two sets of acquisitions of CryoSat-2 data have been used. The results that depend on the measurements of the echo cross-product (sections III-E, IV-A and IV-B) were obtained from acquisitions of SIRAL SARIN mode data observed between 27th July, 2010 and 28th July, 2010 from the Pacific and Indian Oceans. The satellite tracks from which these are taken are a subset of those shown in fig. 2 of [31]. For this study, the data acquisitions falling on orbit numbers 1595, 1599, 1601, and 1607 were used. These data were processed using version Vk 1.0 of the Level 1b processor (used by ESA for the distribution of CryoSat data products from February, 2012 to April, 2013) and the data we used were the SARIN mode L1b data product [41].

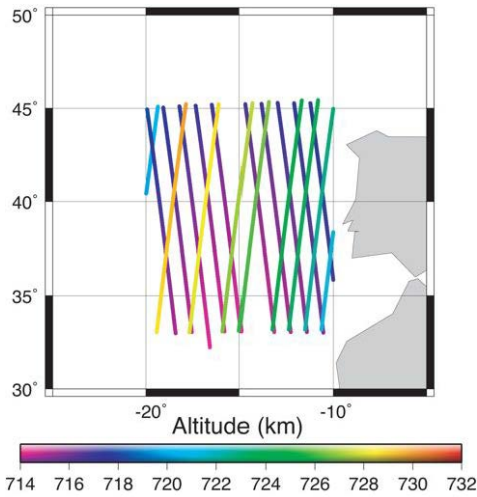


Fig. A1. The location and altitudes of the SAR mode acquisition used in this study. The grey area on the right of the plot are the Iberian Peninsula and the northwest Africa.

For the results that concern the SAR mode and pulse-limited echoes, the data we used were SIRAL SAR mode acquisitions observed from a region off the coast of Portugal in the North Atlantic between the 4th and the 29th of January 2011. (This region was chosen by ESA mission management as providing for a wide range of ocean sea states whilst falling within the operational constraints of data storage and downlink capability.) The location of the satellite tracks during these acquisitions is given in fig. A1. These data were also processed using version Vk 1.0 of the Level 1b processor, from which was obtained SAR mode Level 1b data [41].

In addition to the SAR Level 1b data, we also obtained from the same acquisitions the set of so-called ‘CFBR’ data. These data have the same format as the ESA ‘FBR’ data [41] save that, in addition, they have had applied the full set of internal range, amplitude, phase and phase difference corrections that are generated from the on-board internal calibration measurements. It is from the CFBR data that we obtained the

‘pulse-limited’ data that is described in the main text.

In SAR mode, SIRAL uses a so-called ‘closed-burst’ operation in which groups, or bursts, of pulses are transmitted at intervals long enough that the echoes from earlier bursts can be received. A single burst consists of 64 phase coherent echoes received at the antenna at a burst-repetition frequency (BRF) of 87.5 Hz, with an individual pulse repetition frequency (PRF) set at 18.182 kHz. (Each burst is of 3.14 ms duration, with an inter-burst interval of 11.7 ms.) It is these data, with internal calibrations applied, and with orbit and datation information added, that form the CFBR data.

In the processing of SAR mode L1b data, the echoes received from each burst are processed by performing a ‘range FFT’ (completing the pulse compression of the altimeter) and performing the so-called ‘azimuthal’ FFT. The azimuthal FFT has the effect of focusing the echoes into 63 ‘beams’ directed at consecutive strips on the surface. (While the FFT generates 64 ‘beams’, one of these is as the Nyquist Doppler frequency, and cannot be unambiguously associated with either a forward or backward looking beam.) Echoes from successive bursts directed at the same strip on the surface are grouped, or ‘stacked’, corrected for their slant range (sometimes termed ‘delay compensated’), incoherently detected, and then summed, or ‘multi-looked’ to reduce the speckle noise. The number of non-zero beams, or ‘number of looks’ in each stack is approximately 240 (in detail the number depends weakly on the altitude). Each multi-looked, ‘Level 1b’ echo is present in the L1b data for each strip along-track. These are separated at approximately 300 m along the track, and, at a satellite ground velocity of 6700 ms⁻¹ (that is, the speed with which the nadir point moves over Earth’s surface) occur at a rate of approximately 22 Hz. (A more detailed description of the processing applied to the data can be found in [23])

In SARIN mode, the burst rate is reduced by a factor of 4 of compared with that of the SAR mode and there are 61 looks in the multi-looked echo cross-product at 20 Hz. The SARIN echo power, however, sums incoherently the power received on each antenna, and thus in this case there are 122 looks.

If, however, the processing is interrupted following the range FFT, the burst consists of 64 echoes that have arisen from a conventional, pulse-limited geometry. These echoes can be incoherently detected, and summed, to provide a multi-looked, pulse limited echo at a rate of 87.5 Hz. In our processing, we determine a ‘retracking’ correction, using an OCOG retracker [42], at an 87.5 Hz rate. These corrections are smoothed with a Gaussian filter whose bandwidth is equivalent to 1 Hz, and its outcome is used to align the 87.5 Hz echoes, which are then further summed to generate multi-looked, pulse-limited echoes at a rate of 22 Hz. Each 22 Hz echo is then the result of 256 looks. This data set then comprises the ‘pulse-limited’ echoes referred to in the main text. There is not a one-to-one correspondence between the ‘Level 1b’ SAR mode echoes and the pulse-limited echoes, because the rate of the former is determined by the distance along-track that separates the strips, whereas the latter is determined by the burst timing. They are, however, surveying the same track over the ocean at the same time, and at a

similar rate. For simplicity, we refer to both sets of echoes as occurring at 20 Hz.

The theory of section II assumes that either the pitch, or the pitch and roll, are small, and that the relative variations of the satellite altitude and velocity are small. Table A.1 provides the range of these parameters for the two data acquisitions that we use. With regard to the pitch and roll angles reported in the L1b data products, these are known to be affected by static biases. We have applied a correction of -0.1062 degrees to the roll angles [28] and of -0.055 degrees to the pitch angles [31] to account for these biases.

Table A1. Variations in altitude, altitude rate, satellite speed, pitch and roll.

Altitude	Altitude rate	Satellite speed	Pitch	Roll
km	m s ⁻¹	km s ⁻¹	degrees	degrees
SAR Mode Acquisitions				
714 – 730	-7.50 – 17.0	7.52 – 7.54	-0.7 – -0.02	-0.15 – 0.01
SARIN Mode Acquisitions				
721 – 735	-20.2 – 21.2	7.51 – 7.53	-0.02 – 0.05	-0.09 – 0.32

APPENDIX B. MODEL FITTING AND POST PROCESSING OF THE CRYOSAT DATA.

The calculation of the models of (21) and its SAR and pulse-limited equivalents were performed using the computational package Mathematica. The numerical integrations of (1), (10) and (13) were performed using the routine NIntegrate. Intermediate results (such as the functions J in eqn. (13)), and the final numerical functions (the functions G of (21)), were formed by applying the routine Interpolation to the tabular outcome of the previous numerical integration. We established, by trial and error, that the sampling of the tabular outcome of each integration step was sufficient that the outcome of the succeeding integration differed less than 0.25% when the sampling was further densified. In general, we found that 0.1 ns sampling was sufficient.

The functions $\Psi_r(\tau - \tau_0)$ and $p_r(\tau - \tau_0)$ were fitted to the echo cross-product and echo powers respectively. The free parameters in the fit were the set $\{\tau_0, \sigma_s, \sigma^0, \theta\}$ in the case of the echo cross-product, and $\{\tau_0, \sigma_s, \sigma^0\}$ in the case of the SAR and pulse-limited powers. The values of other parameters that were used in the models are given in Table B1. To fit the echoes, we first non-dimensionalised the echoes using the echo duration and echo amplitude as scale parameters in order that the non-dimensionalised echoes were $O(1)$ in range and amplitude. The non-dimensionalised parameters were chosen so as to minimise the weighted least squares difference between the model and the echo, using as weights the reciprocal of the variances whose determination is described below. In the case of the powers, we used the routine NonLinearModelFit to perform the fit (using the Levenberg Marquardt algorithm); in the case of the cross product, we formed the square of the amplitude of the (complex) difference between the cross-product and the model and used the routine FindMinimum to determine the parameters. (We

did this because the Mathematica routine NonLinearModelFit does not accommodate complex functions. We established, by using this method to fit an example of a (real) power echo, that the two routines returned the same answer for the fit parameters.). Fig. B.1 shows an example of a fit to a 20 Hz echo cross-product, presented in an amplitude and phase representation.

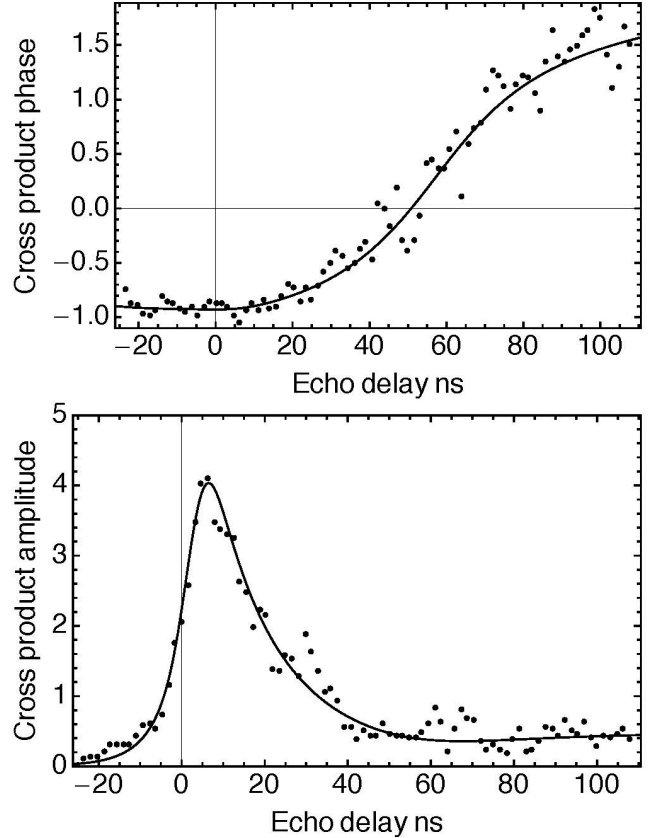


Fig. B1. An example of a fit to a 20 Hz, SARIN mode, echo cross-product. The fitted parameters are $\tilde{\tau}_0 = 1.355$ ns, $\tilde{\sigma}_s = 0.456$ m and $\tilde{\theta} = 0.1638$ degrees. Note that the cross-product phase at zero delay is approximately equal to $k_0 B \theta$, or 0.966 radians (55.35 degrees) in this case. The increase in phase noise at larger delay times – a consequence of the behavior of the cross-product coherence – is visible in the figure.

Table B1. Value of the system parameters used in the model of the echo cross-product and echo power.

Parameter	Symbol	Value
Speed of light	c	2.99792458 m s ⁻¹
Satellite altitude	h_0	720 km
Altitude variation	δ	Variable ⁽¹⁾
Antennas power gain	G_0	42 dB
Earth radius	R	6380 km
Geometric factor	$\eta = 1 + h_0/R$	1.113
Synthetic beam gain	D_0	36.12 dB SAR Mode 30.6 dB SARIN mode
Carrier wavelength	λ	0.022 m
Carrier wavenumber	k_0	285.5 m ⁻¹
Interferometer baseline	B	1.1676 m
Along-track antenna parameter	γ_1	0.0116 radians
Across-track antenna parameter	γ_2	0.0129 radians
Pitch	μ	Variable ⁽¹⁾

Roll	χ	Variable ⁽¹⁾
Satellite speed	v_s	7.53 km s ⁻¹
Number of samples in synthetic aperture	N_a	64
Burst repetition interval	Δ_b	11.7 ms SAR mode 46.7 ms SARIN mode
Pulse repetition interval	Δ_t	55 μ s
Number of looks at 20 Hz	N_s N_{SI} N_p	240 SAR mode 61 SARIN mode 256 pulse-limited

⁽¹⁾Allocated dynamically at 20 Hz rate.

The variances that we used to weight the fit are those of (26). These variances are those of the cross-product or power at fixed values of the echo delay τ . To estimate them from the measurement echoes, the echoes need to be aligned, so that averages are taken across constant values of the echo delay. The shift in delay of the observed echoes needed to achieve this is the value of that arises from the fit, but, in order to obtain this accurately, the weights, and thus variances, must first be determined. Here again, we use an iterative approach, in which we align the echoes using an OCOG retracker [42] to obtain a retracking correction at 20 Hz. The sequence of retracking corrections is then smoothed with a Gaussian filter with a half width equal to 1 s to generate a set of smoothed retracking corrections at 20 Hz. These smoothed corrections are then applied to the 20 Hz data to align them to constant delay time reference. (This smoothing is performed to reduce the noise on the correction resulting from speckle.) Having done that, we then formed estimates of the mean echo, and the variance about the mean, as a function of delay time τ . The variances obtained this way were used to provide weights for the fitting routines, which generated a further sequence of precise retracking corrections at 20 Hz from the values of $\tilde{\tau}_0$ obtained from the fit. This sequence was again smoothed over 1 Hz, and the result reapplied to determine the final sequence of echoes from which the effective number of looks plotted in section III(E) were obtained. (In practice, we did not find that the additional accuracy provided by using the sequence of values of $\tilde{\tau}_0$ made a significant difference to the effective number of looks.)

We applied post-processing editing on the along-track results through “3- σ ” editing of the results by passing them through a 10 s smoothing filter and removing outliers whose residual from the smoothed results exceeded 3 standard deviations of the along-track residual distribution. We also removed values for which the least-square fitting failed to converge. The success with which convergence was achieved was sensitive to the initial values provided to the fit routine as a starting point for its iteration, particularly those of $\tilde{\tau}_0$ and $\tilde{\sigma}_s$. We improved on the success rate by repeating the fits using the smoothed values as a second set of initial values. Following this pass, some 6% of the values we obtained were removed by editing.

To obtain the 1 Hz values of precision described in the text, we separated the sequence of fitted values into 1 second blocks. We fitted a straight line through each 1 second set of 20 Hz values, and took the standard deviation of the residuals

as the measurement precision. While there are alternatives to this piece-wise approach, this method is conventional (R. Scharroo, personal communication) in reporting altimeter precisions.

Details of the method and external data sets used to perform the calibration of the interferometer whose result is shown in fig. 8 is given in [28].

APPENDIX C. THE EFFECT OF ALTITUDE RATE ON SARIN AND SAR MODE ECHO SHAPE.

As noted in the main text, when the satellite velocity vector is not tangential to the surface at the nadir point, the distribution of beam look angles is not symmetric relative to the nadir direction, but around the normal to the velocity vector. Because the synthetic beam gain is modulated by the antenna gain, beams that are formed at angles larger than would otherwise be the case are strongly attenuated by the antenna gain, and accounting for them by extending the summation to include them has little effect on the summation of (3). However, there is a corresponding loss of beams at angles smaller than those included in the summation of (3), and if the altitude rate of the satellite is sufficiently high, the loss of power in the multi-looked echo is sufficient to alter the echo shape in a detectable way. Fig. C1 shows the effect on the SAR mode echo shape of an altitude rate of 40 ms⁻¹. With this altitude rate, the normal to the satellite velocity makes an angle of 0.3 degrees with the nadir direction, and some 10 beams are lost from the summation of (3).

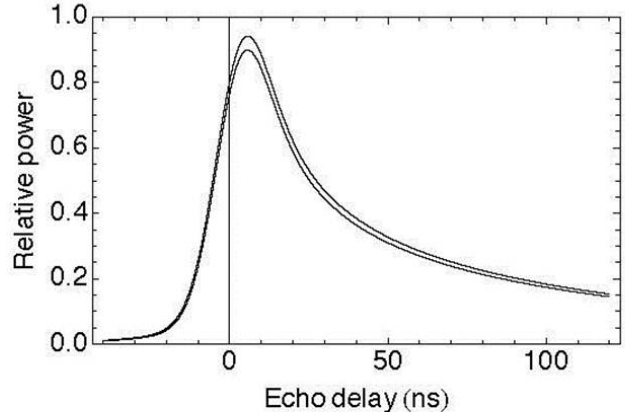


Fig. C1. A comparison of the SAR mode or SARIN mode mean echo power that occurs with an altitude rate of zero and that with an altitude rate of 40 ms⁻¹. When the altitude rate is non-zero, the outer beams are lost from the summation in the multi-looking, resulting in a lower power, and some alteration of the echo shape. The maximum difference is some 4%. The calculation is done for a wave height of 2 m.

The effect increases exponentially with altitude rate, because of the modulation of the antenna pattern. For altitude rates smaller than 20 ms⁻¹, the effect is negligible. In this study, the maximum altitude rate that occurred during the acquisitions was 21.2 ms⁻¹ (table A1) and this rate was rarely encountered,

and we have not accounted for this effect in the models used to fit the data described in this paper. The expected effect on estimated backscatter is small, as the backscatter estimate is dominated by the AGC setting and not the fitted waveform amplitude.

ACKNOWLEDGEMENTS

Many of the results in this paper were presented at the 2011 OSTST meeting (19-21st October, San Diego, CA). The authors would like to thank Laurent Phalippou and Christine Gommenginger for their helpful criticism and advice.

The participation of Walter H. F. Smith does not constitute a statement of policy, decision, or position on behalf of the National Oceanic and Atmospheric Administration or the U.S. Government.

REFERENCES

- [1] J. G. Marsh and T. V. Martin, "The SEASAT altimeter mean sea surface model," *J. Geophys. Res.*, vol. 87, pp. 3269–3280, 1982.
- [2] D. T. Sandwell and W. H. F. Smith, "Marine gravity anomaly from Geosat and ERS 1 satellite altimetry," *J. Geophys. Res.*, vol. 102, no. B5, pp. 10 039–10 054, 1997.
- [3] L. Miller and R. Cheney, "Large-scale meridional transport in the tropical Pacific Ocean during the 1986–1987 El Nino from Geosat," *J. Geophys. Res.*, vol. 95, pp. 17905–17919, 1990.
- [4] R. E. Cheney and J. G. Marsh, "Seasat altimeter observations of dynamic topography in the Gulf Stream region," *J. Geophys. Res.*, vol. 86, no. C1, pp. 473–483, Jan. 1981.
- [5] C. Wunsch and D. Stammer, "The global frequency-wavenumber spectrum of oceanic variability estimated from TOPEX/POSEIDON altimetric measurements," *J. Geophys. Res.*, vol. 100, pp. 24895–24910, 1995.
- [6] Cartwright, D.E. and R. D. Ray, "Oceanic tides from Geosat altimetry", *J. Geophys. Res.* 95(C3): 3069–3090, 1990.
- [7] Rufenach, C.L. and W. R. Alpers, "Measurement of ocean wave heights using the Geos-3 altimeter", *J. Geophys. Res.* 83(C10):5011–5018, 1978.
- [8] Mognard, N.M. and B. Lago, "The computation of wind speed and wave heights from Geos-3 data", *J. Geophys. Res.* 84(B8):3979–3986, 1979.
- [9] Fu, L.-L. and A. Cazenave, *Satellite altimetry and earth sciences, a handbook of techniques and applications*, vol. 69 in Int'l. Geophysics Ser., ed. by R. Dmowska, J.R. Holton and H.T. Rossby, Academic Press, San Diego, 2001. ISBN 0-12-269545-3
- [10] Chelton, D.B., J.C. Ries, B.J. Haines, L.-L. Fu and P.S. Callahan, "Satellite altimetry", in *Satellite altimetry and earth sciences, a handbook of techniques and applications*, L.-L. Fu and A. Cazenave, eds., Int. Geophys. Ser. v69, Academic Press, 2001.
- [11] Lambin, J. R. Morrow, L.-L. Fu, J.K. Willis, H. Bonekamp, J. Lillibridge, J. Perbos, G. Zaouche, P. Vaze, W. Bannoura, F. Parisot, E. Thouvenot, S. Coutin-Faye, E. Lindstrom, and M. Mignogno, "The OSTM/Jason-2 Mission", *Marine Geodesy* 33(Supplement 1):4–25, 2010.
- [12] Choi, K.-R., J.C. Ries, B.D. Tapley, "Jason-1 Precision Orbit Determination by Combining SLR and DORIS with GPS Tracking Data", *Marine Geodesy* 27(1–2):319–331, 2004.
- [13] Haines, B.J., Y. Bar-Sever, W. Bertiger, S. Desai and P. Willis, "One-Centimeter Orbit Determination for Jason-1: New GPS-Based Strategies", *Marine Geodesy* 27(1–2):299–318, 2004.
- [14] Marth, P.C., J.R. Jensen, C.C. Kilgus, J.A. Perschy, J.L. MacArthur, D.W. Hancock, G.S. Hayne, C.L. Purdy, L.C. Rossi and C.J. Koblinsky, "Prelaunch performance of the NASA altimeter for the TOPEX/Poseidon project", *IEEE Trans. Geosci. Rem. Sens.* 31(2):315–332, 1993.
- [15] M. Roca, S. Laxon, and C. Zelli, "The ENVISAT RA-2 instrument design and tracking performance", *IEEE Trans. Geosci. Remote Sens.*, vol. 47, no. 10, pp. 3489–3506, Oct., 2009.
- [16] Raizonville, P., N. Lannelongue, J.C. Anne and P. de Chateau Thierry, "Poseidon solid state altimeter", *Acta Astronautica* 17(1):23–30, 1988;
- contains the proceedings of paper IAF-86-83 presented at the 37th congress of the International Astronautical Federation, Innsbruck, Austria, 4–11 October 1986.
- [17] J. T. McGoogan, "Satellite altimetry applications," *IEEE Trans. Microw. Theory Tech.*, vol. MTT-23, no. 12, pp. 970–978, Dec. 1975.
- [18] MacArthur, J.L., "Design of the SEASAT-A Radar Altimeter", proceedings of the Oceans '76 conference, Washington DC, 13–15 September 1976, Oceans'76:222–229, 1976.
- [19] G. S. Brown, "The average impulse response of a rough surface and its applications", *Antennas and Propagation, IEEE Transactions on*, vol. 25, no. 1, pp. 67–74, Jan. 1977.
- [20] D. J. Wingham, A. J. Ridout, R. Scharroo, R. J. Arthern, and C. K. Shum, "Antarctic elevation change from 1992 to 1996," *Science*, vol. 282, pp. 456–458, 1998.
- [21] Zwally, H.J., Brenner, A.C., Major, J.A., Bindchadler, R.A., Marsh, J.G. Growth of Greenland ice sheet: measurement. *Science* 246, 1587–1589, 1989.
- [22] S. W. Laxon, N. Peacock, and D. Smith, "High interannual variability of sea ice thickness in the Arctic region," *Nature*, vol. 425, pp. 947–950, 2003.
- [23] D. J. Wingham, C. R. Francis, S. Baker, C. Bouzinac, D. Brockley, R. Cullen, P. de Chateau-Thierry, S. W. Laxon, U. Mallow, C. Mavrocordatos, L. Phalippou, G. Raitier, L. Rey, F. Rostan, P. Viau, and D. W. Wallis, "CryoSat: A mission to determine the fluctuations in Earth's land and marine ice fields", *Adv. Space Res.*, vol. 37, no. 4, pp. 841–846, 2006.
- [24] W. T. K. Johnson, "Magellan imaging radar mission to Venus", *Proceedings of the IEEE*, vol. 79, no. 6, pp. 777–790, Jun. 1991.
- [25] Jensen, J.R., "Angle measurement with a phase monopulse radar Altimeter.", *IEEE Trans. Antenn. Propag.* 47, 715–724, 1999.
- [26] R. K. Raney, "The Delay/Doppler Radar Altimeter", *IEEE Trans. Geosci. Remote Sens.*, vol. 36, no. 5, pp. 1578 – 1588, 1998.
- [27] Jensen, J. R., R.K. Raney, "Delay Doppler radar altimeter: Better measurement precision", *Proc. IEEE Geosci. Remote Sens. Symposium IGARSS'98*. Seattle, WA, IEEE: 2011–2013, 1998
- [28] N. Galin, D.J. Wingham, R. Cullen, M. Fornari, W.H.F. Smith, S. Abdalla, "Calibration of the CryoSat-2 Interferometer and Measurement of Across-Track Ocean Slope", *Geoscience and Remote Sensing, IEEE Transactions on*, vol. 51, no.1, pp.57–72, Jan. 2013.
- [29] D. J. Wingham, L. Phalippou, C. Mavrovordatos, and D. Wallis, "The mean echo and echo cross-product from a beam-forming, interferometric altimeter and their application to elevation measurement", *IEEE Trans. Geosci. Remote Sens.*, vol.42, no. 10, pp.2305–2323, Oct. 2004.
- [30] R. K. Raney, "CryoSat SAR-Mode Looks Revisited", *IEEE Trans. Geosci. Remote Sens. Lett.*, Vol. 9, no. 3, pp.393 – 2397, 2012
- [31] N. Galin, D.J. Wingham, R. Cullen, R. Francis, I. Lawrence, "Measuring Pitch of CryoSat-2, Using the SAR Mode of the SIRAL Altimeter", *Geoscience and Remote Sensing, IEEE Transactions on*, submitted.
- [32] D.J. Wingham & D.W. Wallis, "The rough surface impulse response of a pulse-limited altimeter with an elliptical antenna", *IEEE Antennas Propagation Lett.*, Vol. 9, pp. 232 – 235, 2010.
- [33] G. S. Hayne, "Radar altimeter mean return waveforms from near-normal-incidence ocean surface scattering", *Antennas and Propagation, IEEE Transactions on*, vol. 28, no.5, pp.687–692, Sep. 1980.
- [34] P. Beckmann, A. Spizzichino, "The scattering of electromagnetic waves from rough surfaces", Vol. 4, Pergamon Press, 503 p., 1963.
- [35] M. V. Berry, "The Statistical Properties of Echoes Diffracted from Rough Surfaces", *Phil. Trans. R. Soc. Lond. A*, vol. 273, pp 611–654, 1973.
- [36] E. Rodriguez and J. M. Martin, "Correlation properties of Ocean Altimeter Returns", *IEEE Trans. Geosci. Remore Sens.*, vol. 32, no. 3, pp 553 – 561, 1994.
- [37] E. J. Walsh, "Analysis of experimental NRL radar altimeter data", *Radio Science*, volume 9, numbers 8&9, pages 711–722, August–September, 1974.
- [38] E. J. Walsh, "Pulse to pulse correlation in satellite radars", *Radio Science*, volume 17, number 4, pages 786–800, Julpy–August, 1982.
- [39] N. K. Pavlis, S. A. Holmes, S. C. Kenyon, and J. K. Factor, "An earth gravitational model to degree 2160: EGM 2008," presented at the European Geosciences Union (EGU) General Assembly, Vienna, Austria, Apr. 13–18, 2008. [Online]. Available: <http://earth-info.nga.mil/GandG/wgs84/gravitymod/egm2008/index.html>
- [40] W.H.F. Smith, R. Scharroo, "Retracking range, SWH, sigma-naught, and attitude in CryoSat conventional ocean data", *Ocean Surface Topography Science Team Meeting*, San Diego, 19–21 Oct. 2011.

- [41] CryoSat Product Handbook, [Online]. Available: <http://emits.esa.int/emits-doc/ESRIN/7158/CryoSat-PHB-17apr2012.pdf>
- [42] D.J. Wingham, C.G. Rapley, H. Griffiths, "New techniques in satellite altimeter retracking systems", *Proc. IGARSS'86 Symp.*, Zurich, 1986.